Liu *et al.*
Chinese Journal of Mechanical Engineering (2022) 35:150
https://doi.org/10.1186/s10033-022-00823-z

Chinese Journal of Mechanical Engineering

ORIGINAL ARTICLE

Open Access

A Novel Braking Control Strategy for Hybrid Electric Buses Based on Vehicle Mass and Road Slope Estimation

Zijun Liu[1], Shuo Cheng[1*], Jinzhao Liu[2], Qiong Wu[3,4], Liang Li[1] and Huawei Liang[4]

Abstract

Proper braking force distribution strategies can improve both stability and economy performance of hybrid electric vehicles, which is prominently proved by many studies. To achieve better dynamic stable performance and higher energy recovery efficiency, an effective braking control strategy for hybrid electric buses (HEB) based on vehicle mass and road slope estimation is proposed in this paper. Firstly, the road slope and the vehicle mass are estimated by a hybrid algorithm of extended Kalman filter (EKF) and recursive least square (RLS). Secondly, the total braking torque of HEB is calculated by the sliding mode controller (SMC), which uses the information of brake intensity, whole vehicle mass, and road slope. Finally, comprehensively considering driver's braking intention and regulations of the Economic Commission for Europe (ECE), the optimal proportional relationship between regenerative braking and pneumatic braking is obtained. Furthermore, related simulations and experiments are carried out on the hardware-in-the-loop test bench. Results show that the proposed strategy can effectively improve the braking performance and increase the recovered energy through precise control of the braking torque.

Keywords: Hybrid electric bus, Vehicle mass estimation, Road slope estimation, Braking control strategy, Regenerative braking

1 Introduction

Hybrid electric vehicles (HEVs) have attracted the interest of many original equipment manufacturers and researchers due to their low fuel consumption advantages [1–4]. HEVs can combine the advantages of fuel engines and electric motors, and can achieve braking energy recovery through a regenerative braking system, which further improves fuel economy [5]. In addition, combined with *X*-by-wire technologies such as steer-by-wire (SBW) and brake-by-wire (BBW), HEVs can achieve more precise vehicle chassis dynamics control. Among them, the brake-by-wire system is the main research content of this paper. Through the coordinated distribution of braking force by BBW, the braking safety and energy recovery performance of HEVs can be significantly optimized.

In recent years, many studies focus on maximizing the braking energy recovery efficiency and ensuring braking stays for HEVs. Since the regenerative braking system can only provide a limited electric braking torque, the mechanical braking system should be considered simultaneously. Therefore, designing an appropriate distribution strategy is a crucial technology for HEVs [6–9]. Xu et al. proposed a fuzzy control regenerative braking strategy to distribute the braking force between front and rear wheels, and the braking force on the driving wheels should be within the range allowed by the economic commission of Europe (ECE) regulations as much as possible. Meanwhile, a battery temperature influence factor is designed to modify the calculated regenerative braking force [10]. To recover more braking energy, Lv et al. proposed a synthetic power distribution control strategy

*Correspondence: shuocheng9@yeah.net

[1] State Key Laboratory of Automotive Safety and Energy, Tsinghua University, Beijing 100084, China
Full list of author information is available at the end of the article

considering the braking intension, the wheel speed, and the battery state of charge (SOC) [11]. Gao et al. analyzed the working status and motor characteristics under different braking conditions and proposed three motor dynamic distribution strategies based on different targets. The results of the urban cycle driving simulations showed that the braking energy could be recovered, and the braking system has not been changed too much [12–14].

Vehicle mass and road slope are closely related to the braking performance. Lack of this information may lead to insufficient braking force or an unstable deceleration process. Sun et al. put forward a hybrid estimation method for simultaneously estimating the vehicle mass and road grade in the driving process of hybrid electric buses, but they did not consider the braking process and the energy recovery system [15]. Winstead et al. used an extended Kalman filter (EKF) based method to estimate key parameters online, and then used a model predictive control (MPC) method to track the desired vehicle speed based on these parameters. However, the vehicle mass is assumed to be a constant value without any change [16].

In reality, the total mass of the vehicle varies with the number of passengers, and different roads have different slopes. Due to these uncertain factors, it is difficult to design an optimal braking control strategy [17]. For hybrid electric buses (HEBs), the braking system usually adopts a pneumatic braking scheme, and the control accuracy and response time are not as good as the hydraulic braking system of passenger vehicles. In addition, the driving motor of the bus is usually located on the rear axle, so it is of great significance to study the braking force distribution strategy of different axles and the regenerative braking control strategy [18, 19].

Considering the impact of braking force on the vehicle dynamics system, this paper estimates the vehicle mass and road slope based on a hybrid algorithm of EKF and recursive least squares (RLS). Subsequently, a sliding mode controller is designed to calculate the braking force, while a coordination method of regenerative braking and pneumatic braking is adopted under the conditions allowed by ECE regulations to improve the energy recovery performance.

The rest of this paper is organized as follows: the structure of the braking system and the estimation algorithm are described in Section 2. The sliding mode controller and the braking force distribution strategy are proposed in Section 3. Simulations and experiment results are presented in Section 4. Conclusions are given in Section 5.

2 Vehicle System Modelling

2.1 HEB's Chassis Structure and Whole Control Architecture

The configuration of the HEB braking system is shown in Figure 1. The braking system mainly includes regenerative braking and pneumatic braking. Regenerative braking only acts on the driving wheels (the driving wheels in this paper are the rear wheels), and pneumatic braking can act on all wheels [20–23]. Regenerative braking and pneumatic braking can freely distribute braking torque. When the driver depresses the brake pedal, the micro control unit (MCU) can identify the braking intention and distribute the torque relationship between regenerative braking and pneumatic braking.

By collecting the pedal stroke signal, the total braking force is distributed to the front and rear wheels. After that, the rear wheel braking force is divided into electric motor (EM) and pneumatic braking based on wheel speed information and EM status.

Parameters of the HEB model given by Zhongtong Bus Holding Co., Ltd. are listed in Table 1.

The structure of the control algorithm for the braking force of the HEB is shown in Figure 2. First of all, the mass and the road slope are estimated by EKF and RLS. After that, the total braking torque is calculated from the desired deceleration. Then the braking torque is distributed to achieve the goal of tracking the desired deceleration while ensuring energy recovery.

2.2 HEB's Longitudinal Dynamics Model

As shown in Figure 3, the HEB's longitudinal dynamics model considering the influence of braking force is as follows [23]:

$$\delta m \frac{\mathrm{d}v}{\mathrm{d}t} = F_\mathrm{t} - F_\mathrm{f} - F_\mathrm{w} - F_\mathrm{i} - F_\mathrm{b}, \tag{1}$$

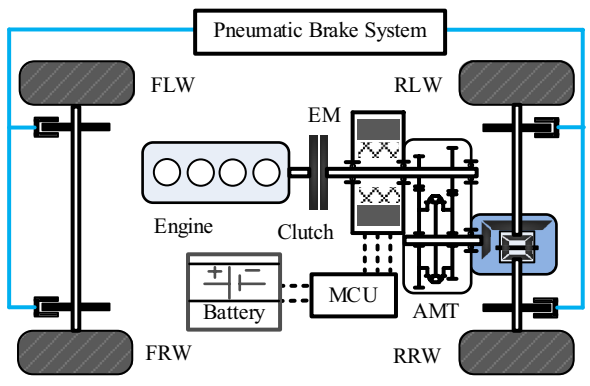

Figure 1 Chassis structure of the HEB

Table 1 Main parameters of the HEB

Components	Description
Engine	Type: Inline six-cylinder diesel engine; Displacement: 1.9 L; Maximum power: 170 kW; Maximum speed: 2400 r/min; Peak torque: 850 N·m
EM	Type: permanent magnet synchronous motor (PMSM); Maximum power: 130 kW; Maximum speed: 3000 r/min; Peak torque: 1100 N·m
AMT	Gear ratio: [6.39, 3.97, 2.4, 1.48, 1, 0.73]; Final drive ratio: 5.57; Average efficiency: 0.9
Battery	Type: NiMH Spiral Wound; Nominal cell voltage: 1.2 V; Total cells: 480; Nominal voltage: 345 V; Capacity: 13 A·h
Vehicle	Mass: 13500 kg; Frontal area: 3.66 m^2; Air resistance coefficient: 0.44; Road resistance coefficient: 0.013; Tire radius: 0.517 m; Tire inertia: 4.829 kg·m^2 for each. Wheelbase: 4.65 m; Gravity center height: 2 m

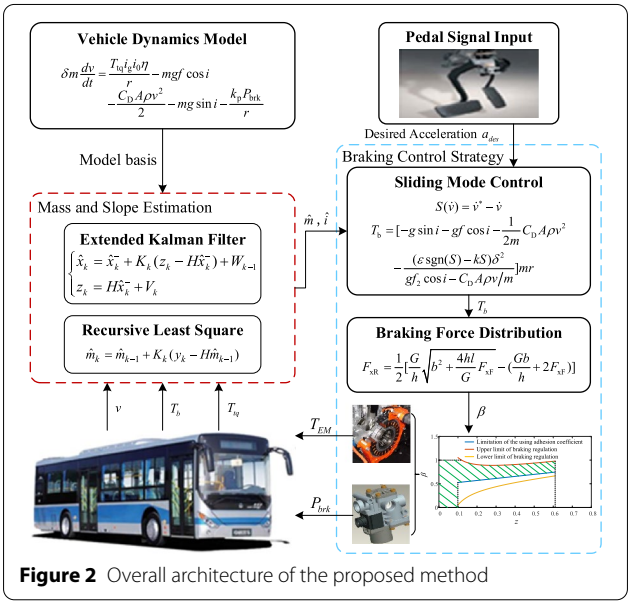

Figure 2 Overall architecture of the proposed method

where δ, m, and v are the rotational mass conversion factor acceleration, the vehicle mass, and the longitudinal speed, respectively. F_t is the driving force of the vehicle, F_f, F_i, F_w, and F_b are the rolling resistance, the slope resistance, the air resistance, and the braking force, respectively. In Figure 3, a, b are the distances from the vehicle gravity center to the front and rear axles, respectively. l is the wheelbase and h_g is the height of the vehicle gravity center.

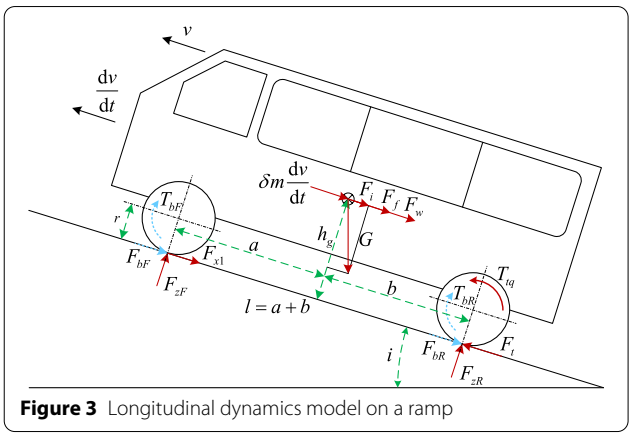

Figure 3 Longitudinal dynamics model on a ramp

After expanding the expression of Eq. (1), the vehicle longitudinal dynamics equation can be expressed as:

$$\begin{aligned}\delta m\frac{\mathrm{d}v}{\mathrm{d}t} =& \frac{T_{\mathrm{tq}}i_{\mathrm{g}}i_0\eta}{r} - mgf\cos i \\ &- \frac{C_{\mathrm{D}}A\rho v^2}{2} - mg\sin i - \frac{k_{\mathrm{p}}P_{\mathrm{brk}}}{r},\end{aligned} \tag{2}$$

where T_{tq} is the driving torque, and it can be the braking torque generated by the EM when the vehicle needs, i_{g} is the gearbox ratio, i_0 is the final drive ratio, η is the mechanical transmission efficiency, r is the wheel rolling radius, f is the coefficient of the rolling resistance, i is the road gradient, C_{D} is the drag coefficient, A is the frontal area, ρ is the air density, k_{p} is the torque conversion factor and P_{brk} is the brake chamber pressure.

In the normal driving process of urban buses, the longitudinal speed will not change significantly due to the small braking force and wheel slip ratio [21]. Therefore, the vehicle speed can be equivalently obtained by the wheel speed. At this point, the mass and road slope can be estimated by EKF and modified by RLS based on our previous research [15].

2.3 Hybrid Estimation Method of Mass and Slope

The longitudinal speed v, the whole vehicle mass m, and the road gradient i are selected as the state variables of EKF. Hence, the state vector of the system is defined as $x(k) = [v(k), m(k), i(k)]^{\mathrm{T}}$. The mass of the vehicle can be regarded as constant when driving in a sampling interval (0.1 s), and the road gradient changes slowly under one sampling interval. The derivative of both is approximated to zero, and the differential equations can be expressed as:

$$\begin{cases} \dot{v}(k) = \left[\dfrac{T_{\mathrm{tq}}(k) i_{\mathrm{g}} i_0 \eta}{m(k) r} - g \sin i(k) - gf \cos i(k) \right. \\ \qquad \left. - \dfrac{C_{\mathrm{D}} A \rho v^2(k)}{2m(k)} - \dfrac{k_{\mathrm{p}} P_{\mathrm{brk}}}{m(k) r}\right] / \delta, \\ \dot{m}(k) = 0, \\ \dot{i}(k) = 0. \end{cases} \tag{3}$$

After time Δt, the discrete state-space model of the system can be obtained by:

$$\begin{cases} v_k = v_{k-1} + \Delta t[\dfrac{T_{\mathrm{tq}}(t_{k-1}) i_{\mathrm{g}} i_0 \eta}{m_{k-1} r} - g \sin i_{k-1} \\ \qquad - gf \cos i_{k-1} - \dfrac{C_{\mathrm{D}} A \rho v_{k-1}^2}{2m_{k-1}} - \dfrac{k_{\mathrm{p}} P_{\mathrm{brk}}}{m_{k-1} r}] / \delta, \\ m_k = m_{k-1}, \\ i_k = i_{k-1}, \end{cases} \tag{4}$$

where Δt represents the sampling interval as 0.1 s.

It is assumed that the process noise and measurement noise of the system are additive noise. The process noise vector and measurement noise vector are $\boldsymbol{W}_k$ and $\boldsymbol{V}_k$ respectively, which are mutually independent and have a mean Gaussian white noise.

The state-space expression of the EKF system is as follows:

$$\begin{cases} \hat{x}_k = \hat{x}_k^- + \boldsymbol{K}_k (z_k - \boldsymbol{H} \hat{x}_k^-) + \boldsymbol{W}_{k-1}, \\ z_k = \boldsymbol{H} \hat{x}_k^- + \boldsymbol{V}_k, \end{cases} \tag{5}$$

where $\boldsymbol{H} = [1, 0, 0]$ is the chosen observation matrix.

The vehicle mass m and the road slope i are estimated according to EKF, which includes two calculation processes: time update and measurement update. The flow chart of the EKF algorithm is shown in Figure 4.

Equations of the time update process can be written as:

$$\hat{x}_k^- = f(\hat{x}_{k-1}), \tag{6}$$

$$\boldsymbol{P}_k^- = \boldsymbol{J}_f(\hat{x}_{k-1}) \boldsymbol{P}_{k-1} \boldsymbol{J}_f^{\mathrm{T}}(\hat{x}_{k-1}) + \boldsymbol{Q}_{k-1}, \tag{7}$$

where $\boldsymbol{P}_k^-$, $\boldsymbol{J}_f$, $\hat{x}_k$, $\boldsymbol{P}_{k-1}$, $\boldsymbol{Q}_{k-1}$ represent the error covariance matrix of the last step, Jacobian matrix obtained by partial derivative of process equation vector function on state variables, optimal prediction of observer estimation, last moment error covariance, and covariance matrix of noise process, respectively.

In this estimation algorithm, it is available in Eq. (8):

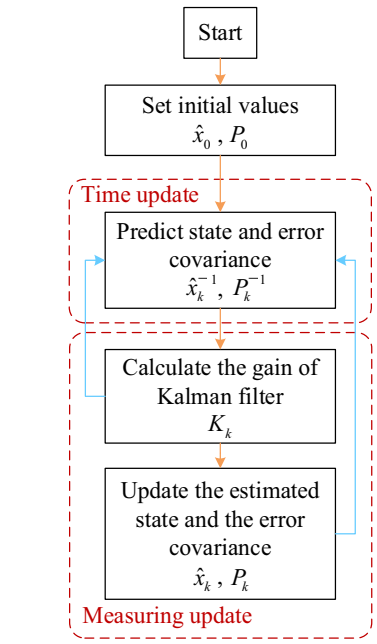

Figure 4 Flow chart of the EKF algorithm

$$\boldsymbol{J}_f = \begin{pmatrix} \frac{\partial f_1}{\partial v} & \frac{\partial f_1}{\partial m} & \frac{\partial f_1}{\partial i} \\ \frac{\partial f_2}{\partial v} & \frac{\partial f_2}{\partial m} & \frac{\partial f_2}{\partial i} \\ \frac{\partial f_3}{\partial v} & \frac{\partial f_3}{\partial m} & \frac{\partial f_3}{\partial i} \end{pmatrix} = \begin{pmatrix} \boldsymbol{A} & \boldsymbol{B} & \boldsymbol{X} \\ 0 & 1 & 0 \\ 0 & 0 & 1 \end{pmatrix}, \tag{8}$$

where,

$$\boldsymbol{A} = \left(-g f_2 \cos i - C_{\mathrm{D}} A \rho v / m\right) \Delta t / \delta,$$

$$\boldsymbol{B} = \left(C_{\mathrm{D}} A \rho v^2 r - 2 T_{\mathrm{tq}} i_{\mathrm{g}} i_0 \eta\right) \Delta t \Big/ 2 m^2 r \delta,$$

$$\boldsymbol{X} = (-g \cos i + g f \sin i) \Delta t / \delta.$$

The measurement update process of the algorithm can be written as:

$$\boldsymbol{K}_k = \boldsymbol{P}_k^- \boldsymbol{H}^{\mathrm{T}} (\boldsymbol{H} \boldsymbol{P}_k^- \boldsymbol{H}^{\mathrm{T}} + \boldsymbol{R})^{-1}, \tag{9}$$

$$\hat{x}_k = \hat{x}_k^- + \boldsymbol{K}_k (z_k - \boldsymbol{H} \hat{x}_k^-), \tag{10}$$

$$\boldsymbol{P}_k = (\boldsymbol{I} - \boldsymbol{K}_k \boldsymbol{H}) \boldsymbol{P}_k^-, \tag{11}$$

where $\boldsymbol{K}_k$, $\hat{x}_k$, $\boldsymbol{P}_k$, and $\boldsymbol{I}$ represent the gains of Kalman filter, optimal estimation of observed variables, error covariance of observer estimation, and identity matrix, respectively.

2.4 Modified Mass Estimation Algorithm Using RLS

In this section, the recursive least square (RLS) method with a forgetting factor is used to establish a modified model of mass estimation based on the longitudinal dynamics model.

Rewrite Eq. (2) into the form that satisfies the requirement of RLS:

$$\begin{aligned} &\underbrace{T_{\mathrm{tq}} i_{\mathrm{g}} i_0 \eta / r - 0.5 C_{\mathrm{D}} A \rho v^2 + T_{\mathrm{b}} / r}_{y_k} = \\ &m \underbrace{[gf \cos i + g \sin i + \dot{v}]}_{H_k}, \end{aligned} \tag{12}$$

where y_k, $\boldsymbol{H}_k$, m are the system output, observable data vector, and system parameters to be estimated. Therefore, the recursive format of vehicle mass can be given as follows:

$$\hat{m}_k = \hat{m}_{k-1} + \boldsymbol{K}_k (y_k - \boldsymbol{H} \hat{m}_{k-1}). \tag{13}$$

The gain matrix $\boldsymbol{K}_k$ and error covariance matrix $\boldsymbol{P}_k$ are:

$$\boldsymbol{K}_k = \frac{\boldsymbol{P}_{k-1} \boldsymbol{H}_k}{\boldsymbol{H}_k^{\mathrm{T}} \boldsymbol{P} \boldsymbol{H}_k + \lambda}, \tag{14}$$

$$\boldsymbol{P}_k = \frac{(\boldsymbol{I} - \boldsymbol{K}_k \boldsymbol{H}_k^{\mathrm{T}}) \boldsymbol{P}_{k-1}}{\lambda}, \tag{15}$$

where λ is the forgetting factor of the RLS model. To decrease the instability of the estimation, the arithmetic uses the lesser forgetting factor. Because of the changing mass of the HEB, the forgetting factor is adjusted, and the error covariance matrix is increased when the velocity of the HEB is 0 m/s. The flow chart of RLS is shown in Figure 5.

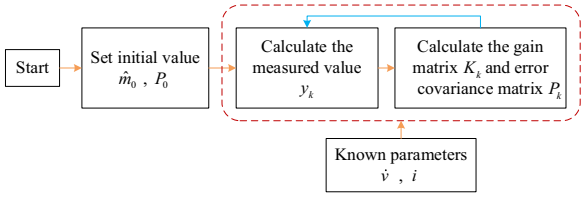

Figure 5 Flow chart of the RLS algorithm

3 Braking Force Distribution Strategies

After estimating the mass and road slope, the total braking force is calculated based on the desired acceleration from the brake pedal signal input by a sliding mode controller. Then, the total braking force is distributed to the front and rear wheels according to the ECE regulations, and a regenerative braking system is adopted on the driving wheels (rear wheels) to recover energy.

3.1 Calculation of the Total Braking Torque

Define the sliding surface as:

$$S(\dot{v}) = \dot{v}^* - \dot{v}, \tag{16}$$

where $\dot{v}^*$ is the desired acceleration, and $\dot{v}$ is the actual acceleration.

An exponential approach rate method is used, which is proposed as follows:

$$\dot{S} = -\varepsilon \mathrm{sgn}(S) - kS, \ \varepsilon > 0, K > 0. \tag{17}$$

The acceleration of the vehicle is defined as:

$$\dot{v} = \frac{-g \sin i - gf \cos i - C_{\mathrm{D}} A \rho v^2 / 2m - T_{\mathrm{b}} / mr}{\delta}, \tag{18}$$

where T_{b} is the sum of regenerative braking torque and friction braking torque. Take the derivative of Eq. (16), and combine Eq. (17):

$$\dot{S} = -\ddot{v} = -\varepsilon \mathrm{sgn}(S) - kS. \tag{19}$$

Finally, the calculated output braking torque is:

$$T_{\mathrm{b}} = \left[-g \sin i - gf \cos i - \frac{1}{2m} C_{\mathrm{D}} A \rho v^2 - \frac{(\varepsilon \mathrm{sgn}(S) - kS) \delta^2}{gf \cos i - C_{\mathrm{D}} A \rho v / m} \right] mr. \tag{20}$$

3.2 Ideal Braking Force Distribution (I Curve)

According to the force analysis of the HEB in Figure 3, the vertical forces of the front and rear axles are as follows:

$$\begin{cases} F_{\mathrm{zF}} = mg(b \cos i + \varphi h \cos i + \sin i) / l, \\ F_{\mathrm{zR}} = mg(a \cos i - \varphi h \cos i - \sin i) / l. \end{cases} \tag{21}$$

When the front and rear axles are locked simultaneously, the use of road adhesion and braking stability is the most advantageous [24–26]. At this time, the ideal braking force relationship between the front and rear axles can be expressed as:

$$\begin{cases} F_{xR} + F_{xF} = \varphi G, \\ F_{xF} = \varphi F_{zF}, \\ F_{xR} = \varphi F_{zR}, \end{cases} \tag{22}$$

$$\frac{F_{xF}}{F_{xR}} = \frac{b\cos i + \varphi h\cos i + \sin i}{a\cos i - \varphi h\cos i - \sin i}, \tag{23}$$

where F_{xR}, F_{xF} are the braking force of the front and rear axle, φ represents the adhesion coefficient of the road surface. If the road gradient is zero, the rear wheel braking force is shown in Eq. (24):

$$F_{xR} = \frac{1}{2}\left[\frac{G}{h}\sqrt{b^2 + \frac{4hl}{G}F_{xF}} - \left(\frac{Gb}{h} + 2F_{xF}\right)\right]. \tag{24}$$

3.3 Front and Rear Axle Braking Force Distribution

The braking force distribution coefficient β of this paper can be expressed as:

$$\beta = \frac{F_{xF}}{F_{xF} + F_{xR}}. \tag{25}$$

In order to ensure the driving safety of the vehicle, a series of requirements are put forward for the braking force of the front and rear axles [27–29]. When the braking intensity z is between 0.1 and 0.61, the utilization adhesion coefficients of the front and rear axles must meet the requirements of Eq. (26):

$$\begin{cases} \varphi_f \le (z + 0.07)/0.85, \\ \varphi_r \le (z + 0.07)/0.85, \\ \varphi_f \ge \varphi_r, \end{cases} \tag{26}$$

where φ_f is the front axle utilization adhesion coefficient, φ_r represents the rear axle utilization adhesion coefficient, z represents the braking intensity.

$$\begin{cases} \varphi_f = \dfrac{F_{xF}}{F_{zF}} = \dfrac{\beta z l}{b\cos i + zh\cos i + \sin i}, \\ \varphi_r = \dfrac{F_{xR}}{F_{zR}} = \dfrac{(1-\beta) z l}{a\cos i - zh\cos i + \sin i}. \end{cases} \tag{27}$$

According to Eqs. (25)–(27), the distribution coefficient β for the ECE regulation can be calculated:

$$\begin{cases} \beta \le (z + 0.07)(b\cos i + zh\cos i + \sin i)/0.85zl, \\ \beta \ge 1 - (z + 0.07)(a\cos i - zh\cos i + \sin i)/0.85zl, \\ \beta \ge b\cos i + zh\cos i + \sin i/l. \end{cases} \tag{28}$$

As shown in Figure 6, the relationship between the braking intensity z and the braking force distribution coefficient β can be obtained by taking the vehicle parameters into Eq. (28) when the road slope is 0. The green region in the figure is the feasible region of the distribution coefficient [30].

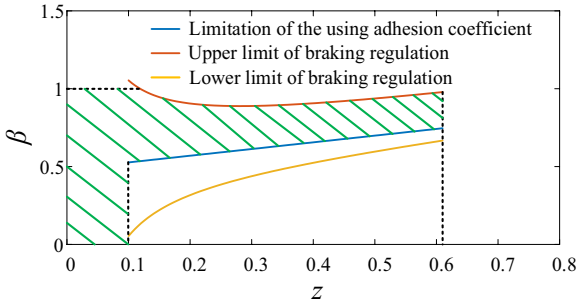

Figure 6 The feasible region of the distribution coefficient

Because the HEB in this paper uses the rear axle drive, the braking force is distributed to the rear axle under the premise of ensuring safety as far as possible to achieve the goal of maximizing the recovery of braking energy while meeting the requirements of the braking regulations.

When the braking intensity is under 0.1, all the braking force is distributed to the rear axle, and the braking force distribution coefficient is 0. When the braking intensity is between 0.1 and 0.61, to guarantee braking safety while maximizing braking energy recovery, the distribution coefficient of the front and rear axle braking forces is calculated using the lower bound of the region in Figure 6. When the road slope is 0, the maximum braking force of the rear axle is as follows:

$$F_{xR\,max} = \begin{cases} Gz, & z \leqslant 0.1, \\ Gz(a - zh)/l, & 0.1 < z < \varphi, \\ G\varphi(a - \varphi h)/l, & z > \varphi, \end{cases} \tag{29}$$

where $F_{xR\,max}$ represents the maximum braking force of the rear axle.

3.4 Regenerative Braking and Pneumatic Braking Force Distribution

After determining the front-to-rear braking axle braking force distribution strategy, the second part of the regenerative braking control strategy is the distribution of the rear axle pneumatic braking force and the regenerative braking force. The coordination between regenerative braking and pneumatic braking uses a coordinated control strategy. The target of the regenerative braking system is to recover the maximum braking energy under the premise of meeting the requirements shown in Eq. (28) and Eq. (29), so the rear axle braking force adopts the following distribution strategy.

If the maximum braking force of EM exceeds the rear axle braking force requirement, the braking force will all be provided by the EM. If the EM's braking force cannot

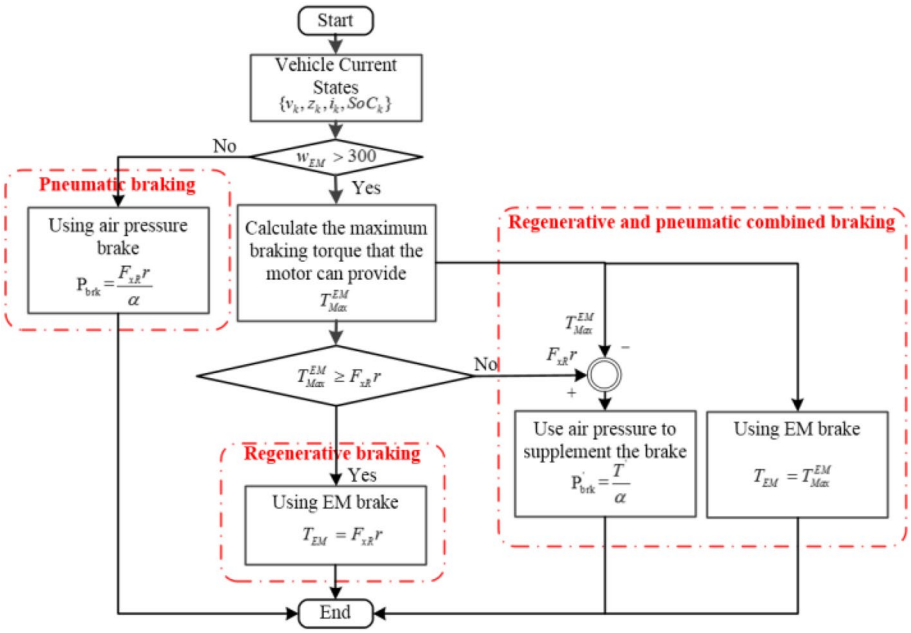

Figure 7 Distribution of regenerative braking and friction braking

meet the rear axle braking force requirements, the maximum EM braking force and the rear axle pneumatic braking force will participate in braking together. The distribution strategy is given in Figure 7.

For the maximum braking torque that the motor can provide, it needs to be calculated based on the characteristics of the EM, current velocity, motor efficiency, and battery status [27–30]. When the vehicle velocity is low, the motor's torque characteristics are unstable, and when the motor is engaged in braking at a low velocity, it consumes electric energy. Therefore, to ensure stable braking performance and reduce energy consumption, regenerative braking is stopped when the motor speed is less than 300 r/min.

4 Simulations and Experiments

To verify the accuracy of the estimation algorithm and the control performance of the braking system, simulations are carried out using MATLAB/Simulink, in which continuously changing road slope and time-varying braking intensity are set. In addition, the mass of the HEB is designed to change when the HEB stops to simulate passengers getting on and off the bus. Finally, the influence of the parameters in the control algorithm and the experimental results are analyzed.

4.1 Simulation of the Hybrid Estimation Algorithm

Figure 8 shows the estimation results of the vehicle mass and road slope by the method proposed in Section 2.

In terms of mass estimation, the error of using the hybrid estimation algorithm is within 3%–4%. Compared with the EKF algorithm alone, the hybrid algorithm has higher stability and precision.

During the whole driving cycle, the slope error estimated by the EKF algorithm is between ± 1.5°, and the responding speed of the changing slope is fast.

4.2 Simulation of the Proposed Braking Force Control Method

In order to compare the effects of the two braking force control algorithms, the same braking intensity is used, as shown in Figure 9.

Actual accelerations under different methods obtained by the simulation and the desired acceleration are shown in Figure 10.

In Figure 10, the acceleration represented by the orange curve is obtained under a fixed vehicle mass and road slope input, while the acceleration represented by the blue curve uses the real-time estimation values as the input of the controller. It can be seen from Figure 10 that when the slope changes and the desired acceleration is small, the actual output acceleration without real-time estimation of vehicle states has obvious chatter compared with the control method proposed in this paper. This will seriously affect the comfort and stability of the HEB. In addition, the actual acceleration under control with vehicle states estimation is closer to the desired value than

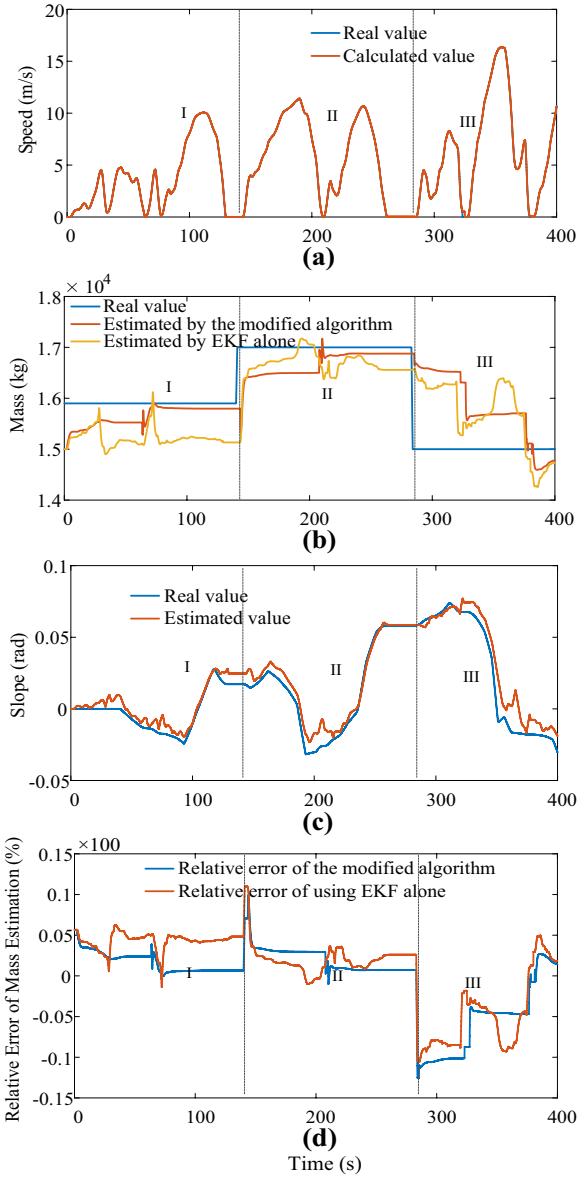

Figure 8 Results of the mass and slope estimation algorithm: (**a**) speed calculation; (**b**) whole vehicle mass estimation; (**c**) road slope estimation, and (**d**) relative error of mass estimation

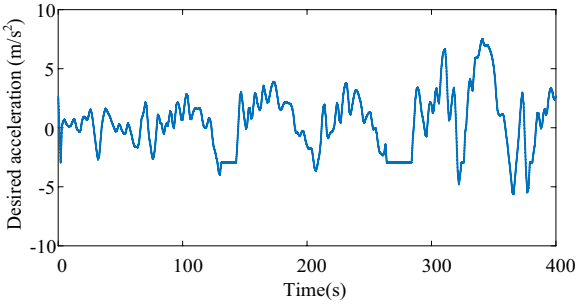

Figure 9 Desired acceleration

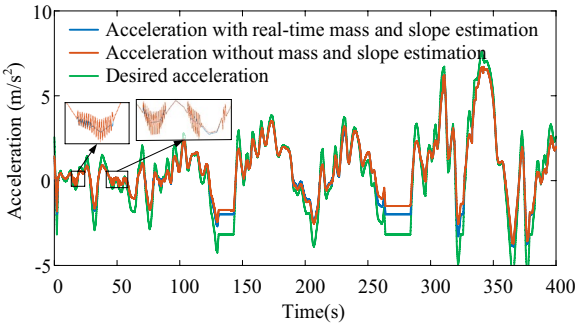

Figure 10 Comparison between actual accelerations and the desired acceleration

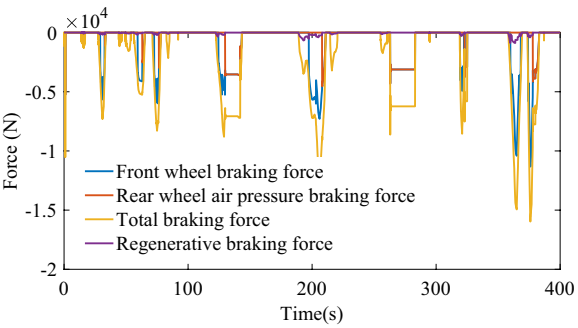

Figure 11 Simulation results of braking force distribution

the actual acceleration without estimation in the region of 120–140 s and 260–280 s.

4.3 Simulation of the Braking Force Distribution Strategy

After determining the total braking force, the braking force of the front and rear wheels and the distribution of regenerative braking and pneumatic braking are performed according to the distribution strategy mentioned. The simulation results of the distribution of braking force are shown in Figure 11.

To compare the results of the battery SoC, three different braking force distribution strategies are set for simulations: the braking force of front and rear axles are distributed according to a fixed ratio, the ideal braking distribution strategy, and the distribution strategy designed in this study. Simulation results of the battery SoC are shown in Figure 12.

At the end of the simulation, the battery SoC using the maximum energy recovery strategy is 0.852, while the battery SoC using the ideal braking force distribution

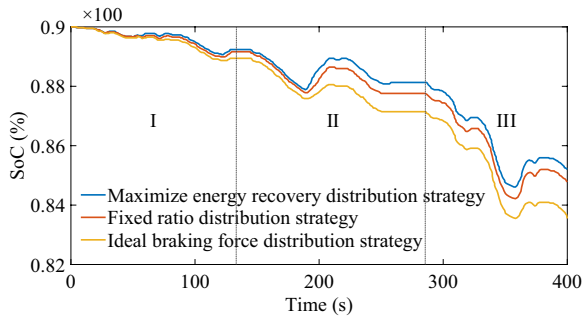

Figure 12 Simulation results of the battery SoC

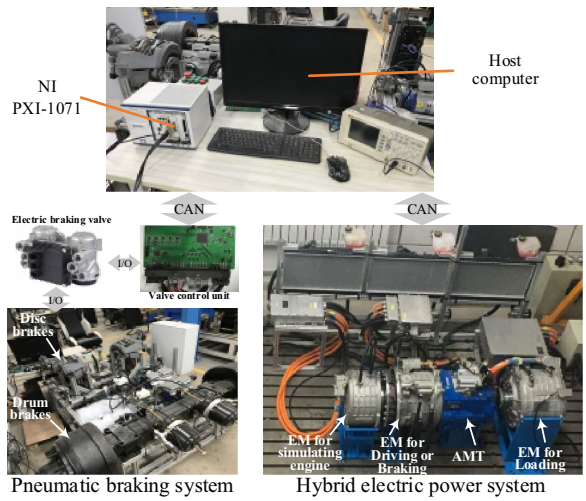

Figure 13 Test bench of the braking system

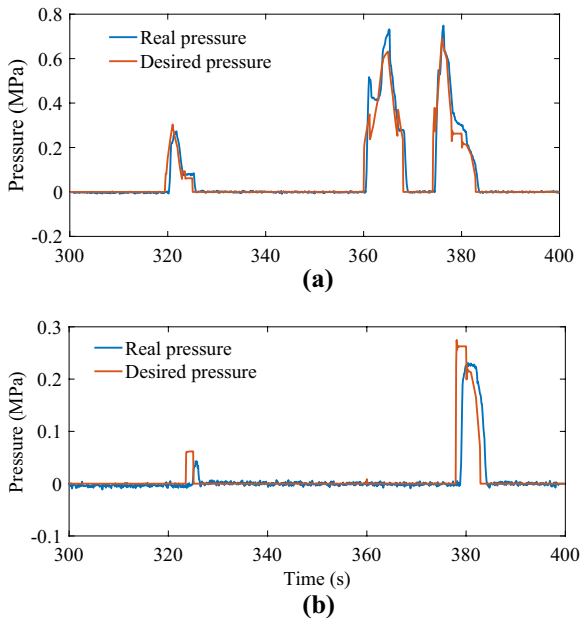

Figure 14 Braking chamber pressure: (**a**) front axle braking chamber pressure; (**b**) rear axle braking chamber pressure

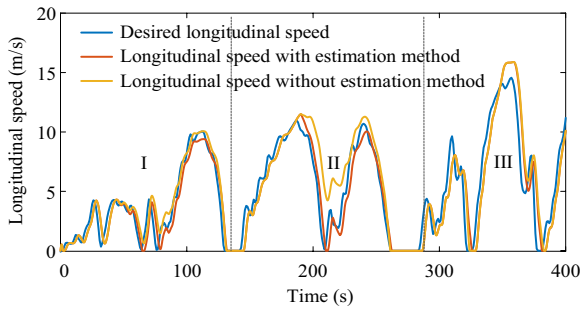

Figure 15 Results of the speed tracking process

strategy is 0.835. The strategy of maximizing energy recovery can relatively increase electrical energy by 2%.

4.4 Experimental Verification

A hardware-in-the-loop (HIL) test bench of the braking system shown in Figure 13 is established to verify the proposed control strategy.

A personal computer (PC) is used as the host computer to display system operating information and download programs to the lower-layer controller. The PXI system of National Instruments serves as a slave computer to run vehicle and motor models, which can collect signals from the test bench and transmit them to the control system in the host computer. The brake-by-wire ECU uses the NXP MPC5744P MCU as the core processor and executes the proposed braking control strategy together with the motor controller through CAN communication.

The pressure curve of the braking chamber and the speed tracking process results are shown in Figures 14 and 15.

The pressure error between the front axle braking chamber and the expected pressure is smaller than that of the rear axle. This is because the pneumatic braking intensity of the rear wheels is low, and there is a delay in the distribution of regenerative braking and pneumatic braking, so the pressure response rate of the rear axle braking chamber is slow.

Speed tracking errors under the same SMC controller can be obtained through the HIL simulation, as shown in Figure 16.

When the actual speed is greater than the desired speed, the speed error is negative, which indicates that the braking performance is not good. In region II, when the time region is within 180–210 s, the braking performance without vehicle mass estimation is worse than the

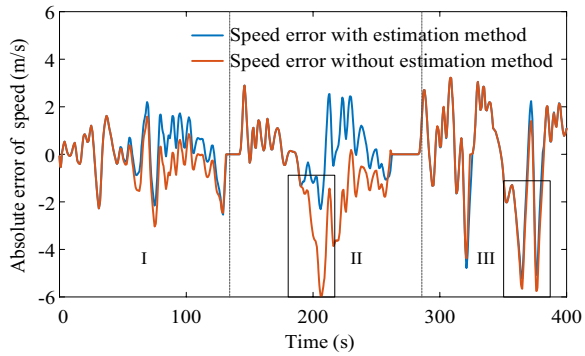

Figure 16 Errors of the speed tracking process

result with the mass estimation algorithm. This is because the whole vehicle mass of the HEB has changed at the beginning of region II. In the time region of 300–400 s, the speed control errors are generally large due to the big braking intensity.

Results show that the proposed real-time control strategy can be implemented and used in actual working conditions and the braking distance of the vehicle can be shortened under the control strategy.

5 Conclusions

This paper proposed an overall control architecture based on the electronically controlled braking system. Firstly, a hybrid estimation method that can estimate both vehicle mass and road slope online is adopted, and the steady-state error of mass estimation can be controlled within 4%. Secondly, a sliding mode controller is used to calculate the total braking force demand based on the braking intensity. Finally, the distribution strategy is proposed to distribute the braking force of the front and rear axles. This strategy can achieve the coordinated control of regenerative braking and pneumatic braking, and improve the energy recovery value by about 2% while optimizing the essential braking ability. In addition, HIL tests indicate that the control architecture has practical application value.

The driving conditions in the real world are very complicated, and curved roads or changing ramps limit the application scenarios of this method. Therefore, future studies will focus on optimizing the estimation performance and considering the impact of road friction coefficient on the braking process.

Acknowledgments
The authors sincerely thank Zhongtong Bus Holding Co., Ltd. for the assistance in experimental tests.

Authors' Contributions
LL and HL were in charge of the whole trial; ZL and SC wrote and revised the manuscript and conducted several simulations; QW assisted in writing the manuscript; JL conceived the method of this paper and assisted in sampling and analysis. All authors read and approved the final manuscript.

Authors' Information
Zijun Liu, born in 1997, is currently a Ph.D. candidate at *State Key Laboratory of Automotive Safety and Energy, Tsinghua University, China*. He received his bachelor's degree from *Hefei University of Technology, China*, in 2019. His research interests include vehicle chassis domain control and intelligent vehicle control.
Shuo Cheng, born in 1994, received his Ph.D. degree at *State Key Laboratory of Automotive Safety and Energy, Tsinghua University, China*, in 2021. He received his bachelor's degree from *Harbin Institute of Technology, China*, in 2016. His research interests include vehicle chassis domain control and intelligent vehicle control.
Jinzhao Liu, born in 1995, received his master's degree from *Beijing Forestry University, China*, in 2020. His research interest includes the electronically controlled braking system of commercial vehicles.
Qiong Wu, born in 1983, is currently a Ph.D. candidate at *Institute of Applied Technology, Hefei Institutes of Physical Science, Chinese Academy of Sciences*, and *University of Science and Technology, China*. His research interest includes intelligent vehicle control.
Liang Li, born in 1978, is currently a tenured professor at *State Key Laboratory of Automotive Safety and Energy, Tsinghua University, China*. His research interests mainly include vehicle dynamics and control, adaptive and nonlinear system control, and the chassis electronic control system of hybrid electric vehicles.
Huawei Liang, born in 1964, is currently a professor at *Institute of Applied Technology, Hefei Institutes of Physical Science, Chinese Academy of Sciences*. His research interests include intelligent vehicle control and artificial intelligence technology.

Funding
Supported by Electric Automobile and Intelligent Connected Automobile Industry Innovation Project of Anhui Province of China (Grant No. JAC2019022505) and Key Research and Development Projects in Shandong Province of China (Grant No. 2019TSLH701).

Competing Interests
The authors declare no competing financial interests.

Author Details
[1]State Key Laboratory of Automotive Safety and Energy, Tsinghua University, Beijing 100084, China. [2]Beijing Forestry University, Beijing 100091, China. [3]University of Science and Technology, Hefei 230026, China. [4]Institute of Applied Technology, Hefei Institutes of Physical Science, Chinese Academy of Sciences, Hefei 230088, China.

Received: 10 November 2022 Revised: 10 November 2022 Accepted: 17 November 2022
Published online: 24 December 2022

References

[1] S Suganya, S Charles Raja, P Venkatesh, et al. Simultaneous coordination of distinct plug-in hybrid electric vehicle charging stations: A modified particle swarm optimization approach. *Energy*, 2017, 138: 92-102.
[2] H Guo, X Wang, L Li, et al. State-of-charge-constraint-based energy management strategy of plug-in hybrid electric vehicle with bus route. *Energy Conversion and Management*, 2019, 199: 11197.
[3] X Wang, L Li, C Yang, et al, Hierarchical control of dry clutch for engine-start process in a parallel hybrid electric vehicle. *IEEE Transactions on Transportation Electrification*, 2016, 2(2): 231-243.
[4] L Li, X Wang, J Song, et al. Fuel consumption optimization for smart hybrid electric vehicle during a car-following process. *Mechanical Systems and Signal Processing*, 2017, 87: 17-29.
[5] S L Zhou, P Walker, N Zhang. Parametric design and regenerative braking control of a parallel hydraulic hybrid vehicle. *Mechanism and Machine Theory*, 2020, 146: 103714.
[6] L Li, X Wang, R Xiong, et al. AMT downshifting strategy design of HEV during regenerative braking process for energy conservation. *Applied Energy*, 2016, 183: 914-925.

[7] J J Zhu, Z P Wang, L Zhang, et al. State and parameter estimation based on a modified particle filter for an in-wheel-motor-drive electric vehicle. *Mechanism and Machine Theory*, 2019, 133: 606-624.
[8] Y Sun, X Wang, L Li, et al. Modelling and control for economy-oriented car-following problem of hybrid electric vehicle. *IET Intelligent Transport Systems*, 2019, 13(5): 825-833.
[9] B Liu, L Li, X Wang, et al. Hybrid electric vehicle downshifting strategy based on stochastic dynamic programming during regenerative braking process. *IEEE Transaction on Vehicular Technology*, 2018, 67(6): 4716-4727.
[10] G Xu, K Xu, C Zheng, et al. Fully electrified regenerative braking control for deep energy recovery and maintaining safety of electric vehicles. *IEEE Transactions on Vehicular Technology*, 2016, 65(3): 1186-1198.
[11] M Lv, Z Chen, Y Yang, et al. Regenerative braking control strategy for a hybrid electric vehicle with rear axle electric drive. *Chinese Automation Congress (CAC)*, Jinan, China, October 20-22, 2017: 521-525.
[12] Y Gao, L Chen, M Ehsani, et al. Investigation of the effectiveness of regenerative braking for EV and HEV. *SAE Transactions*, 1999: 3184-3190.
[13] H Gao, Y Gao, M Ehsani, et al. A neural network based SRM drive control strategy for regenerative braking in EV and HEV//IEMDC. *IEEE International Electric Machines and Drives Conference*, 2001: 571-575.
[14] Y Gao, M Ehsani. Electronic braking system of EV and HEV---integration of regenerative braking, automatic braking force control and ABS. *SAE Transactions*, 2001: 576-582.
[15] Y Sun, L Li, B J Yan, et al. A hybrid algorithm combing EKF and RLS in synchronous estimation of road grade and vehicle mass for a hybrid electric bus. *Mechanical Systems and Signal Processing*, 2016, 68-69: 416-430.
[16] V Winstead, I Kolmanovsky. Estimation of road grade and vehicle mass via model predictive control. *Proceedings of IEEE CCA*, 2005: 1588-1593.
[17] O Hlinka, F Hlawatsch, P M Djuric, et al. Distributed particle filtering in agent networks: A survey, classification, and comparison. *IEEE Signal Proc. Mag.*, 2012, 30(1): 61-81.
[18] Z Mao, B Jiang, P Shi, et al. Fault-tolerant control for a class of nonlinear sampled-data systems via a Euler approximate observer. *Automatic*, 2010, 46(11): 1852-1859.
[19] Y Qin, Z Wang, C Xiang, et al. A novel global sensitivity analysis on the observation accuracy of the coupled vehicle model. *Vehicle Syst. Dyn.*, 2018: 1-22.
[20] Z Chen, R Xiong, J Cao. Particle swarm optimization-based optimal power management of plug-in hybrid electric vehicles considering uncertain driving conditions. *Energy*, 2016, 96: 197-208.
[21] F Sangtarash, V Esfahanian, H Nehzati, et al. Effect of different regenerative braking strategies on braking performance and fuel economy in a hybrid electric bus employing cruise vehicle simulation. *SAE Int. J. Fuels Lubr.*, 2009(1): 828-837.
[22] H Liu, X He, L Chu, et al. Study on control strategy of regenerative braking for electric bus based on braking comfort. *IEEE International Conference on Electronic & Engineering and Information Technology*, 2011: 1037-1040.
[23] X Wu, L Li, X Wang, et al. Nonlinear controller design and testing for chatter suppression in an electric-pneumatic braking system with parametric variation. *Mechanical Systems and Signal Processing*, 2020, 135: 106401.
[24] J J Y Liang, Paul D Walker, J G Ruan. Gearshift and brake distribution control for regenerative braking in electric vehicles with dual clutch transmission. *Mechanism and Machine Theory*, 2019, 133: 1-22.
[25] M Zhou, Z Gao, H Zhang, et al. Research on regenerative braking control strategy of hybrid electric vehicle. *Proceedings of 2011 6th International Forum on Strategic Technology*, Harbin, Heilongjiang, August 22-24, 2011: 300-303.
[26] M Y Yao, D T Qin, X Y Zhou. Integrated optimal control of transmission ratio and power split ratio for a CVT-based plug-in hybrid electric vehicle. *Mechanism and Machine Theory*, 2019, 136: 52-71.
[27] A Eddahec, O Briat, J Vinassa, et al. Performance comparison of four lithium-ion battery technologies under calendar aging. *Energy*, 2015, 84: 542-550.
[28] J J Zhu, Z P Wang, L Zhang. Braking/steering coordination control for in-wheel motor drive electric vehicles based on nonlinear model predictive control. *Energy*, 2019, 142: 103586.
[29] S Cheng, L Li, B Yan, et al. Simultaneous estimation of tire side-slip angle and lateral tire force for vehicle lateral stability control. *Mechanical Systems and Signal Processing*, 2019, 132: 168-182.
[30] X Wang, W Wang, L Li, et al. Adaptive control of DC motor servo system with application to vehicle active steering. *IEEE/ASME Transactions on Mechatronics*, 2019, 24(3): 1054-1063.